Compressible simulations of bubble dynamics with central-upwind schemes

Phoevos Koukouvinis [a, *], Manolis Gavaises [a], Anastasios Georgoulas [b], Marco Marengo [b]

[a] *School of Mathematics, Computer Science & Engineering, Department of Mechanical Engineering & Aeronautics, City University London, Northampton Square EC1V 0HB, United Kingdom*

[b] *School of Computing, Engineering and Mathematics, Cockcroft Building, Lewes Road, University of Brighton, BN2 4GJ Brighton, UK*

*Corresponding author, email: foivos.koukouvinis.1@city.ac.uk,
tel: +44 (0)7561883907

Compressible simulations of bubble dynamics with central-upwind schemes

This paper discusses the implementation of an explicit density-based solver, that utilizes the central-upwind schemes for the simulation of cavitating bubble dynamic flows. It is highlighted that, in conjunction with the MUSCL scheme they are of second order in spatial accuracy; essentially they are high-order extensions of the Lax-Friedrichs method and are linked to the HLL solver family. Basic comparison with the predicted wave pattern of the central-upwind schemes is performed with the exact solution of the Riemann problem, for an equation of state used in cavitating flows, showing excellent agreement. Next, the solver is used to predict a fundamental bubble dynamics case, the Rayleigh collapse, in which results are in accordance to theory. Then several different bubble configurations were tested. The methodology is able to handle the large pressure and density ratios appearing in cavitating flows, giving similar predictions in the evolution of the bubble shape, as the reference.

Keywords: Explicit, compressible, density-based, central-upwind schemes, cavitation, bubble dynamics

1. Introduction

Cavitation is a multiscale phenomenon, involving the extreme growth of initial seeds, voids or cavities within the bulk of a liquid due to the static pressure drop below the saturation pressure (Franc and Michel 2005). The seeds can be of micrometric size, or even lower depending on the quality of the liquid under consideration. The formed cavities are filled with vapour and incondensable, contaminant gases (e.g. atmospheric air) which were dissolved in the liquid. The cavities may exist as long as a low pressure is maintained, forming agglomerations, merging or splitting due to the local flow field, but they collapse soon after pressure recovers.

Traditionally, for the study of cavitation dynamics the Rayleigh-Plesset equation is used (Brennen 1995; Franc and Michel 2005). While the original Rayleigh-Plesset equation was developed with liquid incompressibility as a main assumption (Franc and Michel 2005), extensions exist that allow the incorporation of compressibility and thermal effects, e.g. the Keller variant or the Plesset and Zwick variant, see Brennen 1995. However, either the original Rayleigh-Plesset equation or its more complex variants assume that the bubble shape is perfectly spherical. In practice this is not the case, since many works, experimental (see Obreschkow et al. 2006; Obreschkow et al. 2013) or numerical, (see Hawker and Ventikos 2009; Lauer et al. 2012; Plesset and Chapman 1970; Zhang et al. 2009) suggest that the bubble shape may be strongly deformed in the presence of pressure fields (e.g. due to gravity, due to passing sound waves), or due to the presence of boundaries (walls, free surfaces, etc.). This is especially important in the case of studying cavitation erosion, since the influence of the wall at the bubble development will cause a well-known asymmetric collapse, eventually leading to the microjet effect (Lauer et al. 2012; Plesset and Chapman 1970; Zhang et al. 2009), which is believed to play a fundamental role in erosion, due to the very high pressures that are generated.

Unfortunately, if one wishes to predict the asymmetric bubble collapse, then, due to the aforementioned reasons, it is necessary to do so by properly integrating the Navier-Stokes equations in 2D axis-symmetric or 3D perspective, depending on the exact case and configuration. The complexity of the involved flow pattern is significant, since the flow is multiphase, involving a strongly deforming free surface, very high velocities, due to the microjet, giving rise to very high pressures at the impact site, caused by the well known water hammer effect. Moreover, the flow involves large density ratios of the order of one thousand, making the problem difficult to tackle with standard CFD methods.

Generally, there have been efforts to perform such simulations in the past; one of the first was the pioneering work of Plesset and Chapman 1970 who employed the Marker-and-Cell method for tracking the bubble surface, in order to simulate the collapse of a bubble near a wall. More recent works on the subject of bubble collapse involve the Boundary Element Method (BEM), see the work of Zhang et al. 2009, or the front tracking method of Hawker and Ventikos 2012; while these methodologies provide high fidelity results on the bubble shape, they become problematic when the topology of the bubble surface changes, e.g. when the bubble is transformed to a torus, due to the microjet piercing the bubble.

An alternative to such methodologies is the interface capturing method, where the interface is captured either though the density field itself or by using a phase field or Level Set field. Examples of such works are:

- the work of Adams and Schmidt 2013 or Pohl et al. 2014, where a homogenous equilibrium model is employed for simulating the collapse of cavitation bubbles. Moreover, they employed specialized schemes that ensure consistency at low Mach numbers.
- the work of Lauer et al. 2012, where a non-equilibrium mass transfer model is employed, based on the solution of an additional Level Set field, defining the two compressible states, liquid and vapour.
- the work of Nagrath et al. 2006 where the Level Set approach is used for tracking the bubble interface.

In this work, a method similar to the one used by Adams and Schmidt 2013 and Pohl et al. 2014 will be used; the cavitation bubble will be described as a density difference of a single fluid, governed by a complex equation of state which represents the isentropic phase change due to cavitation. However, in this work the central-upwind schemes shall be used for the flux estimation which, as will be explained later, show a good performance. The aim is to predict the outcome of several different arrangements of bubble collapse near wall configurations, in order to determine the performance of the scheme employed.

2. Numerical methodology

The Euler equations are resolved, considering the influence of cylindrical symmetry, to reduce computational cost. The equations can be written in vector form as:

$$\mathbf{U}_t + \mathbf{F}(\mathbf{U})_x + \mathbf{G}(\mathbf{U})_y = \mathbf{S}(\mathbf{U}) \tag{1}$$

where **U** is the vector of conservative variables, **F** and **G** the flux function and **S** the source term, used to account for cylindrical symmetry around the *y*-axis or spherical symmetry in case of 1D. The formulation of these terms is, see Toro 2009 or LeVeque 2002:

$$\mathbf{U} = \begin{bmatrix} \rho \\ \rho u \\ \rho v \end{bmatrix} \quad \mathbf{F}(\mathbf{U}) = \begin{bmatrix} \rho u \\ \rho u^2 + p \\ \rho uv \end{bmatrix} \quad \mathbf{G}(\mathbf{U}) = \begin{bmatrix} \rho v \\ \rho uv \\ \rho v^2 + p \end{bmatrix} \quad \mathbf{S}(\mathbf{U}) = -\frac{s}{r}\begin{bmatrix} \rho u \\ \rho u^2 \\ \rho uv \end{bmatrix} \tag{2}$$

In the above equations ρ is the density, u, v are the x and y direction velocities respectively, p is the pressure given by the equation of state and r is the radial distance from the axis of symmetry. Indexes t, x and y denote differentiation in respect to time t, x-direction and y-direction respectively. The parameter s in the source term is 2 for spherical symmetry and 1 for cylindrical symmetry. Here, a piecewise barotropic equation of state is used under the Homogenous Equilibrium assumption, which is a combination of the Tait equation of state above saturation and a formula resembling the isentrope within the saturation dome, see Egerer et al. 2014:

$$p(\rho)=\begin{cases} B\left[\left(\dfrac{\rho}{\rho_{sat,L}}\right)^{n}-1\right]+p_{sat} & \rho \geq \rho_{sat,L} \\ p_{sat}+C\left(\dfrac{1}{\rho_{sat,L}}-\dfrac{1}{\rho}\right) & \rho < \rho_{sat,L} \end{cases} \tag{3}$$

In the aforementioned equation B is the liquid bulk modulus, p_{sat} is the saturation pressure, C is a parameter and ρ_{sat} the liquid density at saturation. The values used for the equation of state are summarized in Table 1; values for the pure liquid phase are based on literature, Ivings et al. 1998.

Table 1. Thermodynamic properties for the fluid used in the present study.

Fluid properties		
B	$293.5 \cdot 10^6$	Pa
n	7.15	(-)
$\rho_{sat,L}$	998.2	kg/m^3
C	1450	Pa.kg/m^3
p_{sat}	2339	Pa

In order to evaluate the flux at the interface of the finite volumes, the central-upwind scheme of Kurganov et al. 2001 is used, shown here only for the **F** flux function in 1D:

$$\mathbf{F}_{i+1/2}=\frac{a^{+}_{i+1/2}\mathbf{F}\left(\mathbf{U}^{-}_{i+1/2}\right)-a^{-}_{i+1/2}\mathbf{F}\left(\mathbf{U}^{+}_{i+1/2}\right)}{a^{+}_{i+1/2}-a^{-}_{i+1/2}}+\frac{a^{+}_{i+1/2}a^{-}_{i+1/2}}{a^{+}_{i+1/2}-a^{-}_{i+1/2}}\left(\mathbf{U}^{+}_{i+1/2}-\mathbf{U}^{-}_{i+1/2}\right) \tag{4}$$

and for the local wave speed at the cell interface $a^{+}_{i+1/2}$ and $a^{-}_{i+1/2}$:

$$\begin{aligned} a^{+}_{i+1/2} &= \max\left(u^{+}_{i+1/2}+c^{+}_{i+1/2}, u^{-}_{i+1/2}+c^{-}_{i+1/2}, 0\right) \\ a^{-}_{i+1/2} &= \min\left(u^{+}_{i+1/2}-c^{+}_{i+1/2}, u^{-}_{i+1/2}-c^{-}_{i+1/2}, 0\right) \end{aligned} \tag{5}$$

where the plus/minus signs indicate the direction of interpolation to the cell face; assuming a structured cell arrangement, where cell i-1, i, i+1 are placed in direction of increasing x, plus indicates interpolation towards a positive direction from the i cell towards the cell face i+1/2 located between i, i+1. On the other hand, minus indicates negative direction from the i+1 cell towards the cell face i+1/2 located between i, i+1. Note that the aforementioned formulation is related to the HLL solver, see Brandner et al. 2012. Calculation of the fluxes in 2D is a bit more complicated, since it involves application of Simpson's integration rule at the cell interface, leading to the following relations, see also Figure 1 for the naming convention of the cell interface locations:

$$\mathbf{F}_{i+1/2} = \frac{a^+_{i+1/2,j}}{6\left(a^+_{i+1/2,j} - a^-_{i+1/2,j}\right)}\left[\mathbf{F}\left(\mathbf{U}^{NE}_{i,j}\right) + 4\mathbf{F}\left(\mathbf{U}^{E}_{i,j}\right) + 4\mathbf{F}\left(\mathbf{U}^{SE}_{i,j}\right)\right]$$
$$- \frac{a^-_{i+1/2,j}}{6\left(a^+_{i+1/2,j} - a^-_{i+1/2,j}\right)}\left[\mathbf{F}\left(\mathbf{U}^{NW}_{i+1,j}\right) + 4\mathbf{F}\left(\mathbf{U}^{W}_{i+1,j}\right) + 4\mathbf{F}\left(\mathbf{U}^{SW}_{i+1,j}\right)\right] \quad (6)$$
$$+ \frac{a^+_{i+1/2,j}a^-_{i+1/2,j}}{6\left(a^+_{i+1/2,j} - a^-_{i+1/2,j}\right)}\left[\mathbf{U}^{NW}_{i+1,j} - \mathbf{U}^{NE}_{i,j} + 4\left(\mathbf{U}^{W}_{i+1,j} - \mathbf{U}^{E}_{i,j}\right) + \mathbf{U}^{SW}_{i+1,j} - \mathbf{U}^{SE}_{i,j}\right]$$

and

$$\mathbf{G}_{i,j+1/2} = \frac{a^+_{i,j+1/2}}{6\left(a^+_{i,j+1/2} - a^-_{i,j+1/2}\right)}\left[\mathbf{G}\left(\mathbf{U}^{NW}_{i,j}\right) + 4\mathbf{G}\left(\mathbf{U}^{N}_{i,j}\right) + 4\mathbf{G}\left(\mathbf{U}^{NE}_{i,j}\right)\right]$$
$$- \frac{a^-_{i,j+1/2}}{6\left(a^+_{i,j+1/2} - a^-_{i,j+1/2}\right)}\left[\mathbf{G}\left(\mathbf{U}^{SW}_{i,j+1}\right) + 4\mathbf{G}\left(\mathbf{U}^{S}_{i,j+1}\right) + 4\mathbf{G}\left(\mathbf{U}^{SE}_{i,j+1}\right)\right] \quad (7)$$
$$+ \frac{a^+_{i,j+1/2}a^-_{i,j+1/2}}{6\left(a^+_{i,j+1/2} - a^-_{i,j+1/2}\right)}\left[\mathbf{U}^{SW}_{i,j+1} - \mathbf{U}^{NW}_{i,j} + 4\left(\mathbf{U}^{S}_{i,j+1} - \mathbf{U}^{N}_{i,j}\right) + \mathbf{U}^{SE}_{i,j+1} - \mathbf{U}^{NE}_{i,j}\right]$$

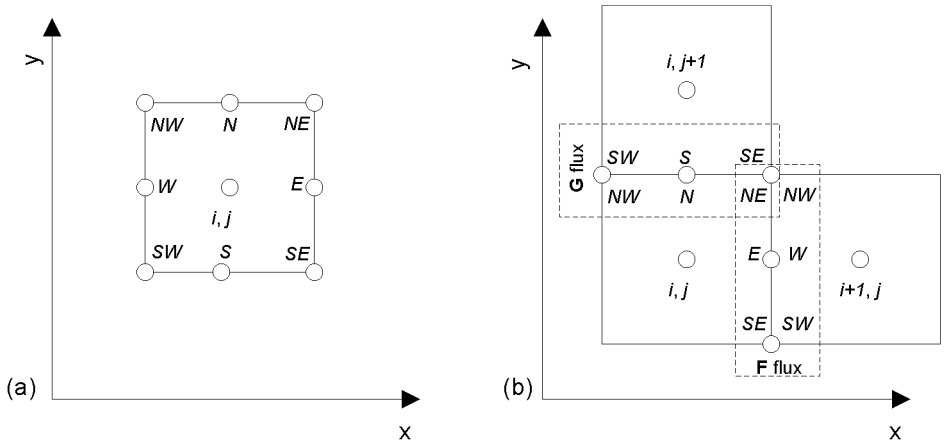

Figure 1. (a) Naming convention of the interface locations used for the cell *i, j* (b) the stencil used for the **F** and **G** flux calculation.

Linear interpolations are used, handled with the MUSCL scheme with a SuperBee limiter, see Toro 2009, though higher-order interpolations could be used for higher accuracy. This scheme has the advantage of being universal, in the sense that it does not need the tuning of the AUSM+up scheme coefficients (see Liou 2006), while it does not require an entropy fix, as e.g. Roe solvers do (Toro 2009). On the other hand, the 2nd (or higher) order extension ensures low numerical diffusion. Boundaries are handled either as transmissive or as rigid slip walls, depending on the configuration (Toro 2009). Viscous and surface tension effects have been omitted. This is justified by the fact that during the bubble collapse velocities of even ~500m/s or more may develop; this leads to Reynolds numbers of ~10^5 or more and Weber numbers of ~10^6. Thus it is safe to assume that viscous and surface tension effects play a minor role in the flow pattern development, which is mainly inertia dominated.

Time integration is performed in an explicit manner, with a splitting scheme Toro 2009, i.e. initially for the homogenous part of eq. 1 and then for the source term. In this work, 1st order Euler integration is used, with a CFL of 0.5, whereas in the future higher order Runge Kutta integration will be implemented.

3. Validation with the exact solver

In Figure 2 the solution of the Kurganov scheme for the Riemann problem with initial conditions ρ_L=1002.88kg/m^3 and ρ_R=9.99kg/m^3, u=0m/s everywhere is shown; also the Lax-Friedrichs and the exact solution are shown for reference. The resolution employed for the numerical methods is 1000 equispaced rectangular finite volumes, while the domain extends from -2m to 2m and the solution is taken at the time instant of 0.5ms. It is of interest that the central-upwind scheme is successful to capture the correct wave pattern, with the same spatial resolution as the Lax-Friedrichs scheme without smearing of the shock, due to the inherent numerical dissipation of the latter. It should be highlighted here that obtaining the exact solution of the Riemann problem is not trivial for arbitrary EOS, such as the one in eq. 3, due to the nature of the Riemann invariants in the rarefaction zone; more details are given in the Appendix section of the present paper and for further clarification the interested reader is addressed to the work of Saurel et al. 1994.

In order to validate the 2D axis-symmetric solver, which will be used later, a comparison with the 1D solver with spherical symmetry was performed. The initial conditions for this comparison are similar to the above, ρ=9.99kg/m^3 for R<1m and ρ_R=1002.88kg/m^3 for R>1m, resembling an implosion configuration. Simulation is performed using 400 finite volumes in the spatial direction, till the time instant of 0.4ms. In Figure 3 the comparison between the 2D axis-symmetric and the 1D spherical symmetric case is depicted, showing perfect agreement.

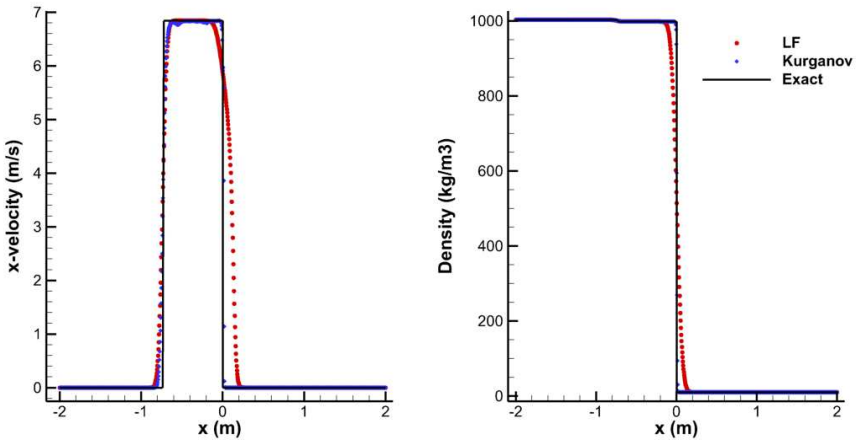

Figure 2. Shock tube test; comparison with exact, Lax-Friedrichs (LF) and Kurganov schemes for cavitating case.

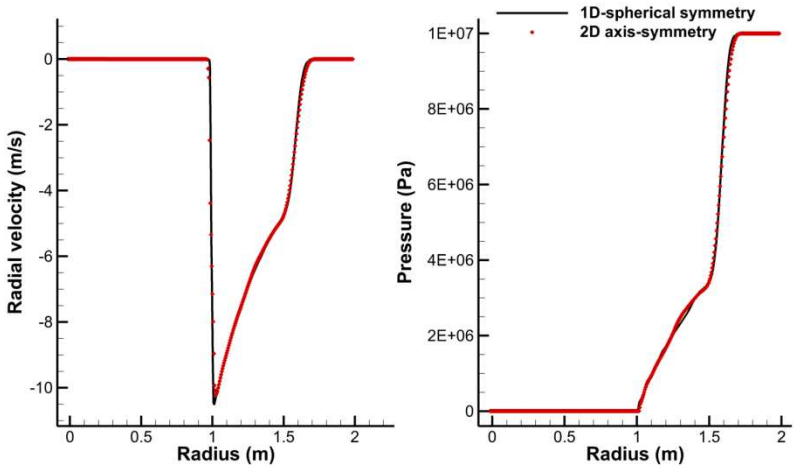

Figure 3. Cavitation implosion simulation with 2D axis-symmetric and 1D with spherical symmetry.

4. Rayleigh collapse test case

Before moving to the more complicated cases such as simulation of a bubble in the vicinity of walls, another fundamental test is performed to assess the behaviour of the central-upwind schemes in the prediction of the inertial vapour collapse; a sphere of vapour is subjected to compression due to the influence of the surrounding high pressure liquid. The configuration resembles the well known Rayleigh collapse, where the radius of the bubble reduces in an accelerating manner, with bubble wall velocity tending to infinity, Franc and Michel 2005. In that case, the bubble collapse velocity is given by the following relation:

$$\frac{dR}{dt} = -\sqrt{\frac{2}{3}\frac{p_\infty - p_v}{\rho}\left[\left(\frac{R_0}{R}\right)^3 - 1\right]} \tag{8}$$

which can be integrated numerically, till the characteristic Rayleigh time τ of bubble collapse:

$$\tau \cong 0.915 R_0 \sqrt{\frac{\rho}{p_\infty - p_v}} \tag{9}$$

In the following figure (Figure 4) the collapse of a vapour bubble with pressure p_v=2173.8Pa, surrounded by liquid of atmospheric pressure 10^5Pa is shown. Both time and radius are non-dimensionalized with the Rayleigh time τ and initial radius R_0 respectively, for clarity. For this simulation, the 1D axis-symmetric solver was employed with spherical symmetry source terms. The total computational domain extends 80 times the initial vapour bubble radius R_0, in order to minimize the interference of the boundaries. Also, to have a high resolution in the bubble region, 12000 control volumes were used (the bubble is initially described by 150 volumes) and a CFL of 0.5 for the time step selection.

As it can be shown from this test, the described methodology is capable of predicting the inertial collapse effects dominating pure vapour structure collapses, in comparison with standard theoretical solution. The low order of accuracy in time integration did not affect the solution quality, since, due to explicit time-stepping, very small time steps had to be used. This gives confidence to proceed further with more complicated cases were theoretical/analytic solutions do not exist.

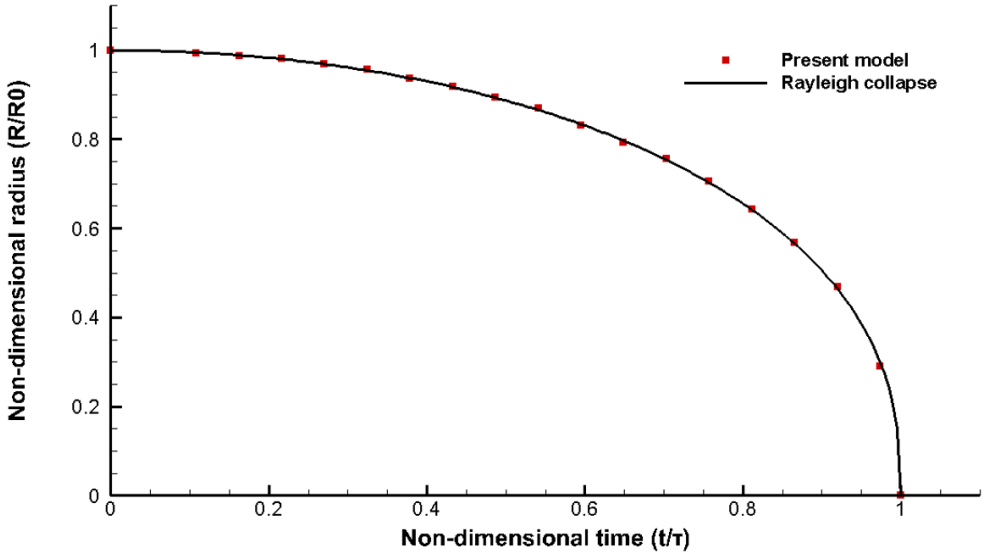

Figure 4. Rayleigh collapse for a bubble of vapour under the influence of higher pressure liquid.

5. Bubble collapse near wall

The case of interest is the collapse of a water vapour bubble in the vicinity of a wall, in the same arrangement as the one used in the work of Lauer et al. 2012, using the framework analyzed in section 2. The bubble has a radius of 400μm and its center is placed at distance d_w = 416, 140 and -140 μm from a wall. The surrounding fluid has a pressure of 100bar, whereas the pressure within the bubble is approximately the saturation pressure i.e. ~2340Pa. The configuration is shown in Figure 5; note that in all further cases the y-axis is the axis of symmetry and the x-axis is the wall. In all cases the computational domain extends 50 times the bubble radius and the bubble is initially described by ~160cells at its radius.

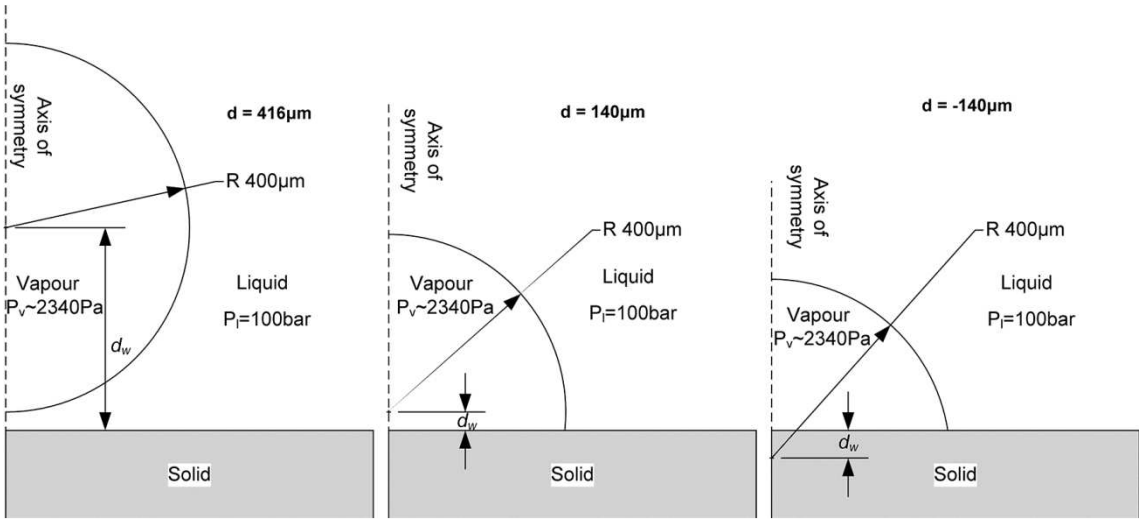

Figure 5. Vapour bubble collapse near a wall configuration

In all the cases to follow, the left image shows the pressure field and the right the velocity magnitude field. The thick black line denotes the vapour/liquid interface at a density of 500kg/m^3, the dashed line the pressure wave location indicated by the pressure gradient magnitude value of ~10^{12}Pa/m and the dashed-dotted line at x=0 is the axis of symmetry. Units are in SI, that is velocity in m/s and pressure in Pa.

In Figure 6 indicative instances of the bubble deformation during the collapse are shown for the d_w=416μm collapse case. At the very early stages of collapse the bubble starts to deform and obtain a non-spherical shape. This is due to the interference of the wall, which prevents the liquid to move towards the bubble. Eventually the collapse is more pronounced at the top of the bubble (see Figure 6b), where momentum focusing occurs and a microjet starts to form, giving the bubble a heart-like shape. At the last stages of collapse the pressure wave emitted from the microjet impact on the wall is evident (see Figure 6c).

In Figure 7, instances during the collapse of the vapour bubble near the wall are shown. As before, the bubble deforms in a non-symmetric manner, due to the microjet effect formed at the axis of symmetry and with a direction towards the wall. Indeed, at later stages the bubble deforms in such a way that a torus attached to the wall is formed, see Figure 7b. At the centre of the torus a high velocity jet impacts the wall, with velocities exceeding 500m/s. Later on, the torus collapses causing high pressures in the vicinity of the microjet impact site as well.

In Figure 8, instances of the bubble collapse for d_w= -140μm; the minus sign means that the bubble centre is below the solid surface. Contrary to the two previous cases, where collapse was biased at the axis of symmetry towards the wall, causing the formation of a microjet effect, here the opposite happens. As it is visible in Figure 8b, in this configuration the collapse is biased on the tangential to the wall direction, giving the bubble a pin-like shape.

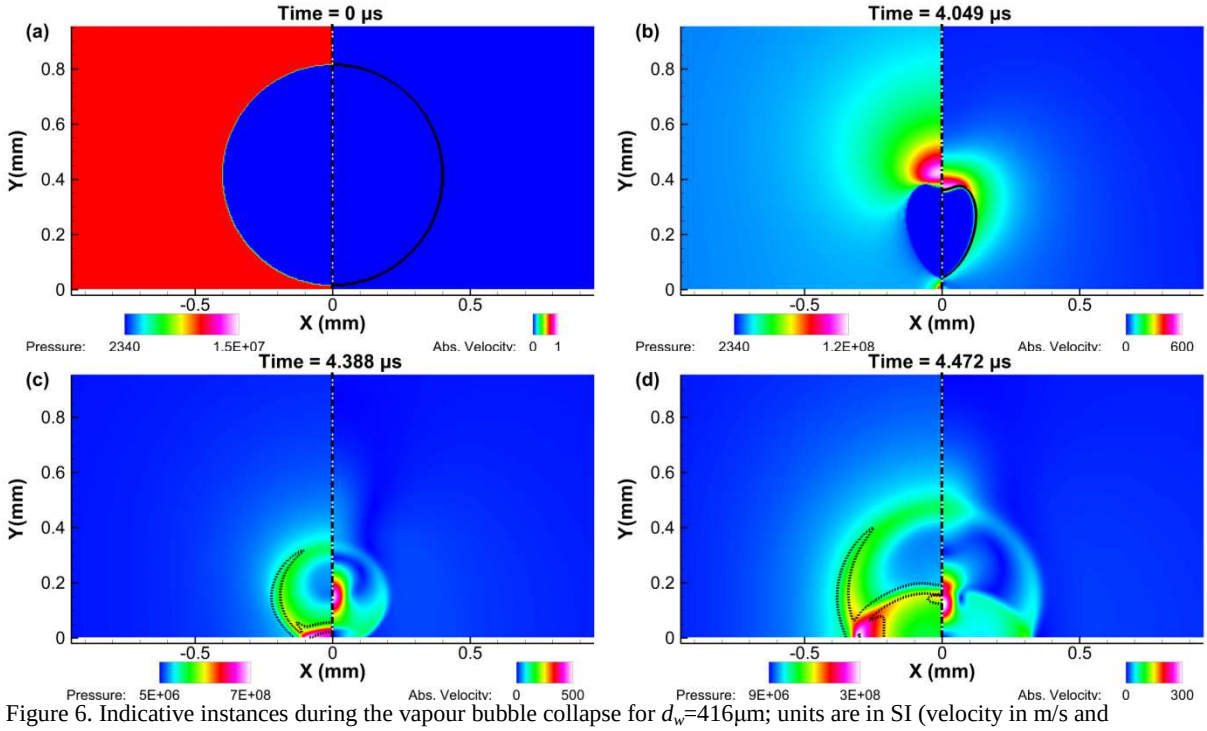

Figure 6. Indicative instances during the vapour bubble collapse for d_w=416μm; units are in SI (velocity in m/s and pressure in Pa). Note the heart-like shape the bubble obtains during the formation of the microjet effect. The dotted line indicates the location of a shock wave, estimated through a pressure gradient isovalue of 10^{12}Pa/m.

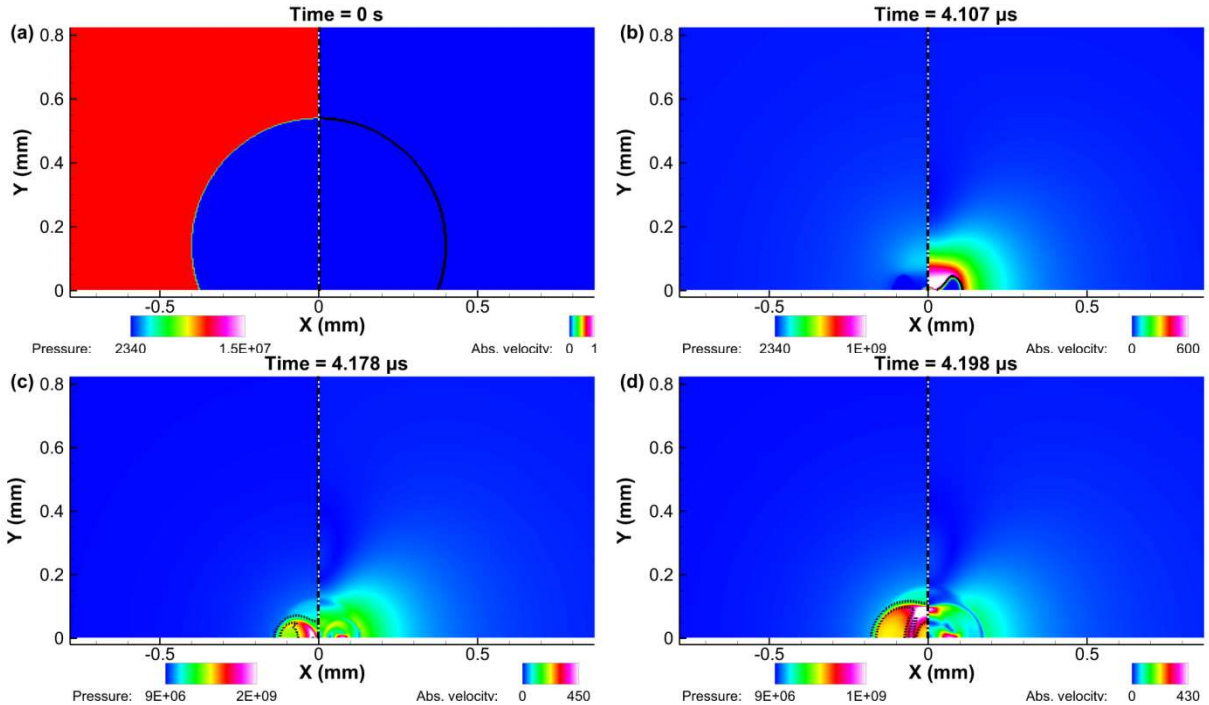

Figure 7. Indicative instances during the vapour bubble collapse for d_w=140μm; units are in SI (velocity in m/s and pressure in Pa). Note the torus shape the bubble obtains during the formation of the microjet effect. The dotted line indicates the location of a shock wave, estimated through a pressure gradient isovalue of 10^{12}Pa/m.

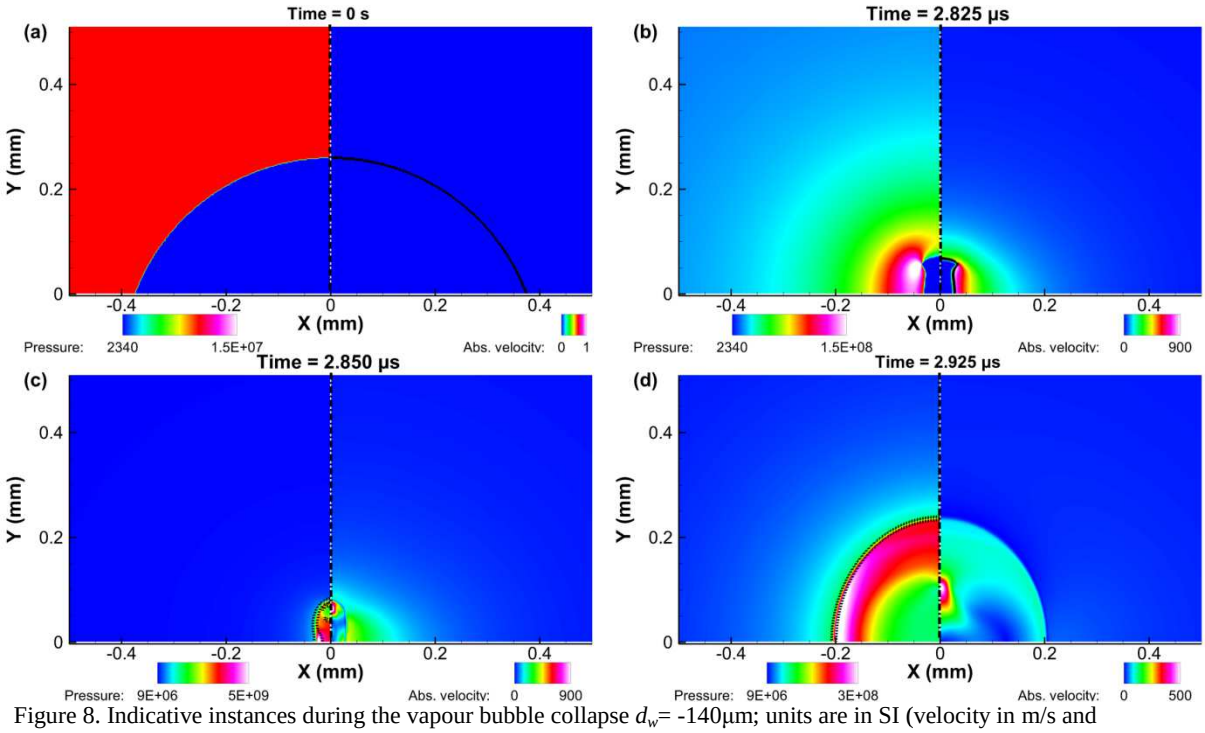

Figure 8. Indicative instances during the vapour bubble collapse d_w= -140μm; units are in SI (velocity in m/s and pressure in Pa). Note the pin-like shape the bubble obtains as it is collapsing. The dotted line indicates the location of a shock wave, estimated through a pressure gradient isovalue of 10^{12}Pa/m.

6. Discussion

It is evident that the wall distance greatly affects the bubble development, in the sense that the initial bubble get deformed due to a jetting phenomenon. When the initial bubble centre is above the wall, then the jet effect is formed on the axis of symmetry, causing the bubble to take a heart like shape or a torus in the cases of 416μm and 140μm respectively. On the other hand, in the case where the initial bubble centre is positioned below the wall, the jet forms in the *x* direction at the wall, deforming the bubble in a pin-like shape. The collapsing times of the bubbles are intuitively reasonable, in the sense that the larger the bubble, the more time it will need to collapse. Indeed the cases with d_w= 416, 140μm and -140μm need approximately 4.3, 4.1 and 2.8μs to collapse respectively; these results are in accordance to the collapse times from the work of Lauer et al. 2012.

The observed collapse pattern can be explained if one considers the angle between the near wall liquid/vapour interface with the wall, see also Figure 9. It has to be kept in mind also that the bubble surface will move locally in the normal to the interface direction, driven be the local pressure difference.

- If the angle between the near wall bubble interface and the wall is less than 90^o, as in cases for d_w=416 and 140μm, then the local velocity can be decomposed to two components; one tangential to wall, with direction towards the axis of symmetry and one normal to wall, with direction away from the wall which tends to detach the liquid from the wall. This causes local depressurization of the liquid and eliminates the pressure difference driving the collapse in the vicinity of the wall. Thus the collapse is more pronounced away from the wall giving rise to the jetting effect.

- On the other hand, if the angle between the near wall bubble interface and the wall is higher than 90^o, as in the case of d_w= -140μm, and by decomposing the local velocity to components tangential and normal to the wall, then the tangential velocity is again towards the axis of symmetry, but now the normal to the wall velocity is towards the wall. This causes a local pressure increase (momentum focusing) which in turn further accelerates the collapse in the tangential to the wall direction and eventually causes the pin type collapse. Needless to say that if the angle between the bubble interface and the wall is exactly 90^o then the collapse will

be spherically symmetric, since this is equivalent of simulating the collapse of a spherical bubble with a symmetry boundary at its middle.

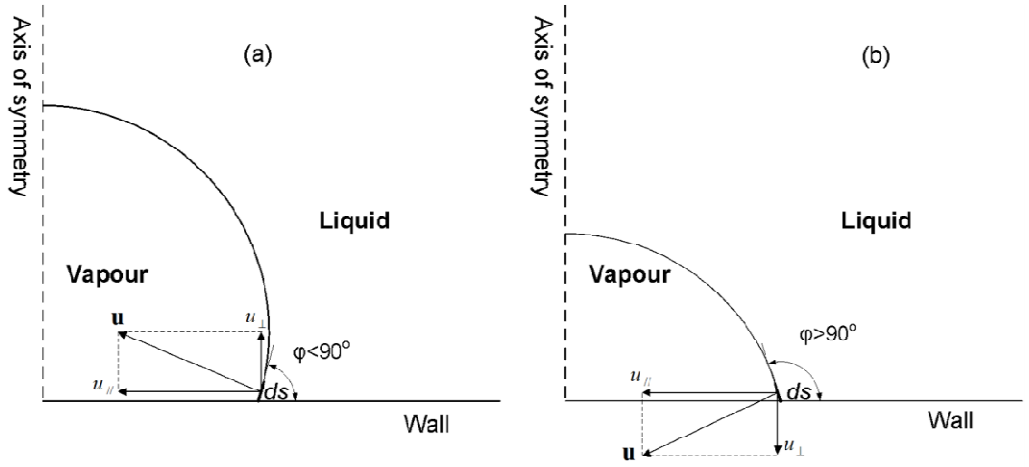

Figure 9. Schematic showing the decomposition of local velocity of the interfacial element *ds* at the vicinity of the wall: (a) corresponds for an arrangement where the bubble centre is above the wall, thus angle $\varphi<90^o$ (b) corresponds for an arrangement where the bubble centre is below the wall, thus angle $\varphi>90^o$. It is apparent that for $\varphi<90^o$ the normal velocity $u_\perp$ is forcing the liquid to detach the wall, whereas for $\varphi>90^o$ $u_\perp$ is towards the wall.

In all cases, the formation of the jet, either on the symmetry axis, or in the *x*-direction causes the development of very high pressures due to momentum focusing. At the late stages of the bubble collapse, the jet will eventually impact on the wall, causing pressures of at least the order of 10000bar, see Figure 10a; such pressures are well beyond the yield stress of many common materials (e.g. SS316L has a yield stress of the order of $2\text{-}4\cdot10^3$bar, see Berchiche et al. 2002), implying that such bubble collapse configurations will contribute to the erosion damage of the underlying solid material. In Figure **10**b, a comparison of the maximum wall pressures with similar values from literature (Lauer et al. 2012) is shown. Apart from an over prediction at d_w=-140μm, a very good match was obtained. It should be highlighted that a similar over prediction was found in the work of Pohl et al. 2014; this could indicate an influence of the Homogenous Equilibrium thermodynamic model.

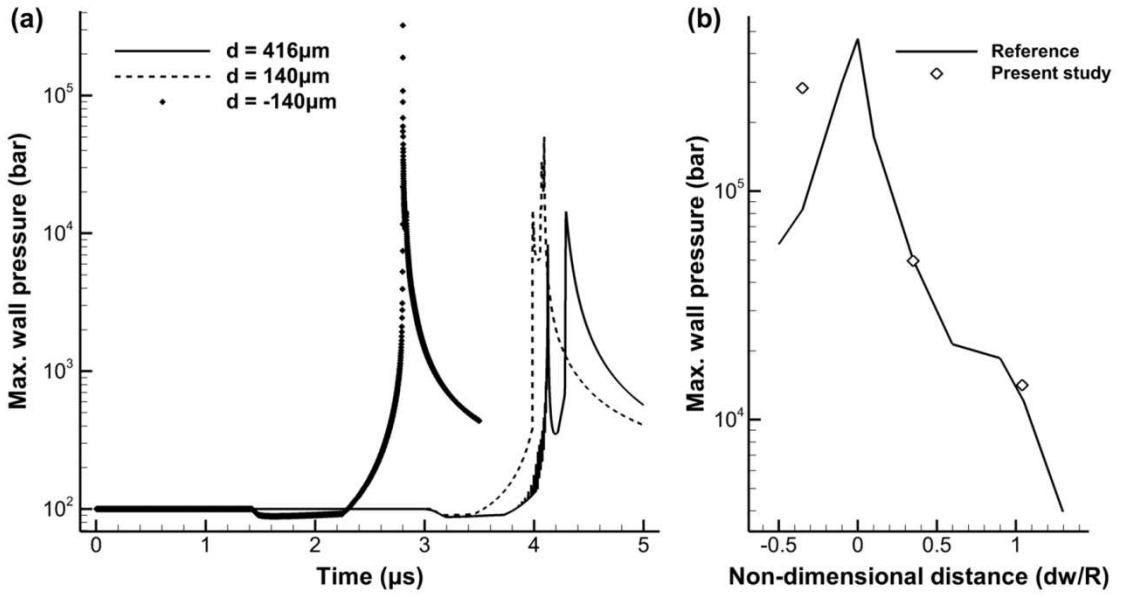

Figure 10. (a) Maximum wall pressure (in bar) at each time step for the examined cases. (b) Comparison of the maximum wall pressure with values from reference (Lauer et al. 2012).

From a numerical point of view, the employed scheme performed well, in the sense that it is able to handle pressure ratios of almost 500000 and density ratios of 1000, without serious problems. High accuracy enabled a clear capturing of the interface within 1-2 cells, without oscillations, thanks to the Total Variation Diminishing properties of the MUSCL scheme. The explicit nature of the scheme allows for fast time marching, with the only restriction being the CFL stability criterion.

7. Conclusion

This paper outlines the development of an explicit density based solver for cavitating flows, based on the central-upwind schemes of Kurganov et al. and the Homogenous Equilibrium assumption, with application on bubble collapse using 2D axis-symmetric conditions; to the authors knowledge central-upwind schemes have not been used in the past in such configurations. The schemes have been tested in comparison with the exact solution of the Riemann problem, showing good accuracy and robustness. Moreover, it is shown that it is possible to predict the inertial collapse effects as has been found with the comparison with the Rayleigh collapse of a vapour bubble. Application of the schemes on the bubble collapse cases showed a similar collapse pattern with the one that has been reported by Lauer et al. and similar pressure levels on the wall, even though a Homogenous Equilibrium assumption is used for the thermodynamic model. One of the main targets in the future is the implementation of higher accuracy in the time marching, specialized low diffusion schemes, and possibly inclusion of thermal effects, with a potential application the simulation of bubble clusters.

Acknowledgements
The research leading to these results has received funding from the People Programme (IAPP Marie Curie Actions) of the European Union's Seventh Framework Programme FP7/2007-2013/ under REA grant agreement n. 324313.

Nomenclature

U	Conservative variable set vector
F	*x*-flux vector
G	*y*-flux vector
S	Source term vector
ρ	Density (kg/m^3)
p	Pressure (Pa)
u	Velocity at x-direction (m/s)
v	Velocity at y-direction (m/s)
s	Geometric source term, unity for cylindrical symmetry and two for spherical symmetry (-)
r	Radial distance from axis of symmetry (m)
B	Bulk modulus of the liquid (Pa)
c	Speed of sound (m/s)
a	Local wave speed (m/s)
R	Bubble radius (m)
d_w	Standoff distance (m)
τ	Rayleigh collapse time (s)

References

Adams, N.A. and S.J. Schmidt, "Shocks in cavitating flows", in *Bubble dynamics & Shock waves*, C.F. Delale, Editor. 2013, Springer-Verlag: Berlin Heidelberg. p. 235-256.

Berchiche, N., J.P. Franc, and J.M. Michel, "A Cavitation Erosion Model for Ductile Materials". *ASME Journal of Fluids Engineering*, 2002. 124: p. 201-207 DOI: 10.1115/1.1486474.

Brandner, M., J. Egermaier, and H. Kopincová, "Numerical Schemes for Hyperbolic Balance Laws – Applications to Fluid Flow Problems", in *Finite Volume Method - Powerful Means of Engineering Design*, R. Petrova, Editor. 2012, InTech.

Brennen, C., "Cavitation and Bubble Dynamics". 1995: Oxford University Press.

Egerer, C., S. Hickel, S. Schmidt, and N. Adams, "Large-eddy simulation of turbulent cavitating flow in a micro channel". *Physics of Fluids*, 2014. 26(085102): p. 30 DOI: 10.1063/1.4891325.

Franc, J.-P. and J.-M. Michel, "Fundamentals of Cavitation". 2005: Kluwer Academic Publishers.

Hawker, N.A. and Y. Ventikos, "Shock/Gas bubble interactions in infinite and finite volumes of liquid", in 2nd Micro and Nano Flows Conference2009: West London, UK.

Hawker, N.A. and Y. Ventikos, "Interaction of a strong shockwave with a gas bubble in a liquid medium: a numerical study". *Journal of Fluid Mechanics*, 2012. 701: p. 55-97 DOI: 10.1017/jfm.2012.132.

Ivings, M.J., D.M. Causon, and E.F. Toro, "On Riemann solvers for compressible liquids". *International Numerical Methods for Fluids*, 1998. 28: p. 395-418 DOI: 10.1002/(SICI)1097-0363(19980915)28:3<395::AID-FLD718>3.0.CO;2-S.

Kurganov, A., S. Noelle, and G. Petrova, "Semidiscrete central-upwind schemes for hyperbolic conservations laws and Hamilton-Jacobi equations". *SIAM Journal on Scientific Computing* 2001. 23(3): p. 707-740 DOI: 10.1137/S1064827500373413

Lauer, E., X.Y. Hu, S. Hickel, and N.A. Adams, "Numerical modelling and investigation of symmetric and asymmetric cavitation bubble dynamics". *Computers & Fluids*, 2012. 69: p. 1-19 DOI: 10.1016/j.compfluid.2012.07.020.

LeVeque, R., "Finite Volume Methods for Hyperbolic Problems ". Cambridge Texts in Applied Mathematics 2002: Cambridge University Press.

Liou, M.S., "A sequel to AUSM, Part II: AUSM+-up for all speeds". *Journal of Computational Physics*, 2006. 214: p. 137-170 DOI: 10.1016/j.jcp.2005.09.020.

Nagrath, S., K. Jansen, R. Lahey, and I. Akhatov, "Hydrodynamic simulation of air bubble implosion using a level set approach". *Journal of Computational Physics*, 2006. 215: p. 98-132 DOI: 10.1016/j.jcp.2005.10.020.

Obreschkow, D., P. Kobel, N. Dorsaz, A. de Bosset, C. Nicollier, and M. Farhat, "Cavitation Bubble Dynamics inside Liquid Drops in Microgravity". *Physical review letters*, 2006. 97 DOI: 10.1103/PhysRevLett.97.094502.

Obreschkow, D., M. Tinguely, N. Dorsaz, P. Kobel, A. de Bosset, and M. Farhat, "The Quest for the Most Spherical Bubble". *Experiments in Fluids*, 2013. 54(4): p. 18 DOI: 10.1007/s00348-013-1503-9.

Plesset, M.S. and R.B. Chapman, "Collapse of an initially spherical vapor cavity in the neighborhood of a solid boundary", 1970, California Institute of Technology. p. 42.

Pohl, F., S. Mottyll, R. Skoda, and Huth, S., "Evaluation of cavitation-induced pressure loads applied to material surfaces by finite-element-assisted pit analysis and numerical investigation of the elasto-plastic deformation of metalic materials ". *Wear*, 2014. 330-331: p. 618–628 DOI: 10.1016/j.wear.2014.12.048.

Saurel, R., M. Larini, and J.C. Loraud, "Exact and approximate Riemann solvers for Real gases ". *Journal of Computational Physics*, 1994. 112(137): p. 12.

Toro, E., "Riemann Solvers and Numerical Methods for Fluid Dynamics: A Practical Introduction". 2009: Springer-Verlag Berlin Heidelberg.

Zhang, A.M., X.L. Yao, and L.H. Feng, "The dynamic behavior of a gas bubble near a wall". *Ocean engineering* 2009. 36: p. 295-305 DOI: 10.1016/j.oceaneng.2008.12.006.

Appendix. Derivation of the exact Riemann Problem solution for an arbitrary equation of state of the form $p=f(\rho)$.

In this section, the methodology for finding the exact solution to the Riemann problem for the Euler equations, for an arbitrary equation of state of the form p=f(ρ) will be outlined, provided that both p, ρ are positive, real numbers. The equation of state could be provided in tabular form. The form of the Riemann problem solved is:

$$\begin{cases} \dfrac{\partial \mathbf{U}}{\partial t} + \dfrac{\partial \mathbf{F}(\mathbf{U})}{\partial x} = 0 \\ \mathbf{U}(x,0) = \begin{cases} \mathbf{U_L} & x < 0 \\ \mathbf{U_R} & x \geq 0 \end{cases} \end{cases} \tag{A.1}$$

where **U**(x,t) is the vector of conservative variables and **F**(**U**) is the flux vector, as shown below:

$$\mathbf{U} = \begin{bmatrix} \rho \\ \rho u \end{bmatrix} \qquad \mathbf{F}(\mathbf{U}) = \begin{bmatrix} \rho u \\ \rho u^2 + p \end{bmatrix}$$

It becomes apparent from the initial conditions that the 1D space has initially a discontinuity at x=0, which separates the domain in two states, the Left (L) and Right (R).
The Jacobian matrix is:

$$\begin{bmatrix} 0 & 1 \\ \dfrac{\partial p}{\partial \rho} - u^2 & 2u \end{bmatrix}$$

where $\sqrt{\dfrac{\partial p}{\partial \rho}}$ is equal to the speed of sound $c(\rho)$.

For positive real, non-zero speed of sound the solution of the Euler equations has two genuinely non-linear waves that can be either shock waves or rarefaction waves. Thus, the solution is self-similar in time and space and is characterized by the velocities of these waves that separate the solution in three states: the Left state, the Right state and the Star state (denoted with '$_*$' from now on) which is unknown. To find it one needs to solve a non-linear algebraic equation for density:

$$g(\rho_*) = g_L(\rho_*) + g_R(\rho_*) + u_R - u_L = 0 \tag{A.2}$$

Functions g_L and g_R depend on the type of non-linear wave. For shock wave the Rankine-Hugoniot
conditions are employed, eventually leading to:

$$g_{K,shock} = \left[\frac{(p_* - p_K)(\rho_* - \rho_K)}{\rho_* \rho_K} \right]^{1/2} \tag{A.3}$$

for *K*=*L* or *R* state.
For the rarefaction wave the Riemann invariants are used, i.e. for left rarefaction wave:

$$du + \frac{c}{\rho} d\rho = 0 \tag{A.4}$$

and for right rarefaction wave

$$du - \frac{c}{\rho} d\rho = 0 \tag{A.5}$$

Integration of these relations is not convenient to be done analytically for a general equation of state, which might be expressed in tabular form. It is rather convenient to perform the integration numerically across the rarefaction wave, as follows for e.g. the left rarefaction wave:

$$u_* - u_L + \int_L^* \frac{c}{\rho} d\rho = 0 \tag{A.6}$$

One can split the integral as follows:

$$u_* + \int_{ref}^{*} \frac{c}{\rho} d\rho = u_L + \int_{ref}^{L} \frac{c}{\rho} d\rho \tag{A.7}$$

where *ref* is a reference state at e.g. the minimum allowable density of the equation of state. In a similar manner one may derive the relation for the right rarefaction wave:

$$u_* - \int_{ref}^{*} \frac{c}{\rho} d\rho = u_R - \int_{ref}^{R} \frac{c}{\rho} d\rho \tag{A.8}$$

and eventually, the function

$$g_{K,rarefaction} = \int_{ref}^{*} \frac{c}{\rho} d\rho - \int_{ref}^{K} \frac{c}{\rho} d\rho \tag{A.9}$$

Hereafter the integral $\int_{ref}^{K} \frac{c}{\rho} d\rho$ will be referred to as $I(\rho_K)$.

Switching between rarefaction and shock wave is done based on pressure:

$$g_K = \begin{cases} g_{K,rarefaction} & p_K < p_* \\ g_{K,shock} & p_K \geq p_* \end{cases} \tag{A.10}$$

For the solution of the Riemann problem, one has to input the equation of state in tabular form, providing pressure *p*, speed of sound *c* and the integral *I* as functions of density. Linear interpolation can be performed to find *p*, *c*, *I* for the calculated density ρ. Care must be taken to have sufficient resolution of the tabular data in areas of steep slope changes, as in the transitions between the piecewise function components of eq. 3, else the interpolation for the speed of sound *c*, or the integral *I* could be very inaccurate.

The solution for the star region can be achieved with the Newton-Raphson method:

$$\rho_n = \rho_{n-1} - \frac{g(\rho_{n-1})}{g'(\rho_{n-1})} urf \tag{A.11}$$

where *n* is the number of the iteration, *urf* is an under-relaxation factor to enhance stability in case of highly non-linear EOS, as in eq. 3, and g' is the derivative of eq. A.2. Note that for such equations it is preferable to resort to a numerically approximated value of the derivative, as:

$$g'(\rho) = \frac{g(\rho + \varepsilon) - g(\rho)}{\varepsilon} \tag{A.12}$$

where ε is a small positive number.

For highly non-linear EOS, it might be preferable also to bound the maximum change of density from iteration to iteration, in order to prevent overshoots/undershoots and enhance stability, i.e.:

$$\rho_n = \max(\min(\rho_n, \rho_{\max}), \rho_{\min})$$

where ρ_{max}, ρ_{min} can be a percentage of density during the previous iteration, e.g. 110% and 90% of ρ_{n-1} respectively. After determining ρ_* within sufficient tolerance, determining velocity u_* is trivial, though the following equation:

$$u_* = 0.5(u_L + u_R) + 0.5[g_R(\rho_*) - g_L(\rho_*)] \tag{A.13}$$

Identification of the type of waves is done depending on pressure at the star region comparing to the left and right states: if $p_* > p_K$ then the wave between the star and *K* region is a shock wave, else it is a rarefaction wave. The type of wave determines the wave speed and the transition between the two states. For a shock wave the transition is sharp and the wave speed is given by:

$$\text{Left shock: } S_L = u_L - \frac{Q_L}{\rho_L}, \text{ right shock } S_R = u_R + \frac{Q_R}{\rho_R} \tag{A.14}$$

with

$$Q_K = \left[\frac{(p_* - p_K)\rho_K \rho_*}{\rho_* - \rho_K} \right]^{1/2} \quad \text{(A.15)}$$

Rarefactions, contrary to shocks, are gradual changes in density, pressure and velocity. Thus, they are associated with two speeds, one for the head of the rarefaction and one for the tail:

$$\text{Left rarefaction, head: } S_{LH} = u_L - c_L \text{ tail: } S_{LT} = u_* - c_* \quad \text{(A.16)}$$

$$\text{Right rarefaction, head: } S_{RH} = u_R + c_R \text{ tail: } S_{RT} = u_* + c_* \quad \text{(A.17)}$$

In order to find the conditions inside the rarefaction wave, the Riemann invariants shall be used. For a left rarefaction, one has to solve the following equation for the point *i* inside the rarefaction:

$$\frac{x_i}{t} + c(\rho_i) + I(\rho_i) = u_L + I(\rho_L) \quad \text{(A.18)}$$

Similarly, for the right rarefaction

$$\frac{x_i}{t} - c(\rho_i) - I(\rho_i) = u_R - I(\rho_R) \quad \text{(A.19)}$$

Solution of eq. A.18 and A.19 can be done numerically, solving for density, using Newton-Raphson method, applying under-relaxation and taking care during the updating of the density values. Experience has shown that it is better to apply a low under-relaxation factor of even 0.02.

Assuming the values from Table I for the EOS (see eq. 1) and assuming an initial discontinuity of the form ρ_L=1002.89g/m^3 for x<0, ρ_R=9.99kg/m3 for x≥0 (which corresponds to p_L=100bar and p_R=2195Pa), one obtains that the solution of the Riemann problem at the star region:

ρ_*=998.200155kg/m^3, p$_*$=2666.7173Pa
u$_*$=6.84509m/s

With rarefaction wave to the left S_{TL}=-1084.66m/s, S_{HL}=-1471.04m/s and shock wave to right S_R=6.91m/s.